ACS Photonics

Open Access

pubs.acs.org/journal/apchd5

Article

Dynamic Control of Topological Charge of Vector Vortex in PCSELs with C_6 Symmetry

Chia-Jui Chang, Yu-Wen Chen, Lih-Ren Chen, Kuo-Bin Hong, Jhih-Sheng Wu, Yao-Wei Huang, and Tien-Chang Lu*

Cite This: *ACS Photonics* 2023, 10, 4112–4120

Read Online

ACCESS | Metrics & More | Article Recommendations | Supporting Information

ABSTRACT: Vortex beams offer significant potential for various applications in fields such as communication, quantum computing, and particle manipulation. Typically, these beams are generated by using laser light that passes through a passive phase modulation component. In recent years, there has been an increasing emphasis on miniaturizing and integrating the vortex beam light source, aimed at expanding the range of applications. Our study contributes to this goal by presenting a novel method for directly generating vector vortex beams from photonic crystal surface emitting lasers while preserving C_6 rotation symmetry. Our approach achieves topological charges of both +1 and −2, and we demonstrate the ability to dynamically switch between these orders by adjusting the injection conditions.

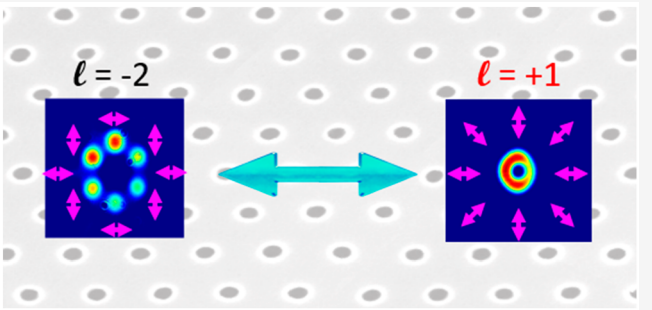

KEYWORDS: *electrically pumped, bound state in continuum, small divergence angle, near-infrared, vector vortex beam light source*

INTRODUCTION

Over the past three decades, significant fundamental studies on vortices have been carried out, and vortex beams have become one of the most important light sources today. A vortex beam (VB) is a type of light that possesses a helical phase front, which corresponds to the orbital angular momentum (OAM) of photons in quantum terms.[1−3] The OAM provides a new dimension of light and has promising applications in many fields. For instance, in optical communication, OAM multiplexing can be combined with traditional multiplexing methods to further increase channel capacity.[4−6] Moreover, the theoretically unlimited quantum number of OAM enables infinite bits to be encoded in a single code unit.[7] In the field of detection, the angular velocity of a rotating body can be obtained by irradiating it with vortex beams and measuring the frequency discrepancy of scattered light caused by the rotating Doppler effect.[8,9] Vortex beams can also transfer OAM to small particles through absorption, which causes the particles to rotate around the optical axis, making vortex beams useful as optical wrenches.[10] Furthermore, the hollow profile of the vortex beam in the transverse direction has led to the discovery of new applications. Optical tweezers, also known as beam-gradient traps, take advantage of the peculiar shape of vortex beams and can trap particles with a lower refractive index than the ambient in the dark core.[11−14] In contrast, optical tweezers that use a Gaussian beam trap particles with a higher refractive index.

In recent years, intensive attention has been focused on the vector vortex beam (VVB). The VVB is a particular class of VB and is characterized by its optical singular center surrounded with an azimuthally twisted polarization. The VVB can be viewed as the superposition of circularly polarized states (which carry spin angular momentum (SAM)) with different OAM values. The spin−orbit nonseparable structure is useful in both classical and quantum fields. Spin-to-orbital angular momentum transfer in nonlinear wave intermixing has been demonstrated with the assistance of the VVB, allowing the information transfer between different degree of freedom of photons.[15] In addition to investigating the entanglement of orbital angular momentum (OAM) and spin angular momentum (SAM) within each vortex vector beam (VVB), research has also explored the entanglement between VVBs, opening up possibilities for various quantum information.[16] On the other hand, the distinct focusing properties of VVBs have also been studied in recent years, leading to various applications. For example, the radially polarized beam can be focused into the so-called "needle beam", which is known for its longitudinal polarization and extended depth of focus,

Received: May 3, 2023
Revised: October 18, 2023
Accepted: October 19, 2023
Published: November 28, 2023

https://doi.org/10.1021/acsphotonics.3c00561
ACS Photonics 2023, 10, 4112–4120

making it useful in applications such as photolithography and microscopy.[17,18]

Due to the promising characteristics of VVBs, many methods have been proposed. The most straightforward method is spatially modulating the polarization of output beams; this is usually achieved with elements like q-plates,[19−21] spatial light modulators,[22,23] and electro-optic crystals.[24] Beside spatially modifying the polarization, VVBs can also be derived by proper design of laser cavity[25,26] or by superposition of two circularly polarized beams with different handedness and topological charges (TCs).[27−29] However, these methods suffer from issues like bulkiness in size, low damage threshold, or low efficiency, limiting their potential applications, such as in consumer electronics or photonic integrated circuits. In recent years, advancements in subwavelength structure technology have led to the emergence of metasurfaces as a new tool for generating vector vortex beams (VVBs). Metasurfaces are able to manipulate the phase and amplitude of light with small size and high efficiency, allowing for the creation of complex wavefronts that can generate VVBs. Compared to traditional methods, using metasurfaces to generate VVBs offers advantages such as higher efficiency and a smaller footprint.[30−39] In addition to metasurfaces, other techniques have also been investigated for generating VVBs. One such method involves the direct generation of VVBs from light sources, which has been achieved through the integration of metasurfaces and vertical-cavity surface-emitting lasers (VCSELs) by Fu et al.[40] Similarly, Cai et al. utilized an angular grating on a ring oscillator to extract light with OAM, resulting in a miniaturized architecture for generating VVBs that can fit within a single chip.[41] However, while metasurfaces and gratings can produce beams with specific OAM values, situations may arise in which it is necessary to adjust the OAM of the resulting beams. Therefore, relying solely on fixed OAM outputs may not always be practical.

Research in the field of photonic crystal (PC) structures has focused on exploring the topological nature of optical bound states in the continuum (BICs). These BICs have been identified as the vortex centers in the polarization direction of far-field radiation.[42,43] Experimental demonstrations have successfully showcased these features in photonic crystal slabs through optical or electrical pumping, and they are regarded as good candidates of VVB sources.[44−50] While VVBs show great promise, significant interest is put on the dynamic switching of the topological charge. Huang et al., in their research,[48] put forth a proposal involving the alteration of the imaginary part of the refractive index, effectively disrupting the symmetries of the structure through control of the optical pumping area. On a different front, Cai et al. delved into the realm of phase-change materials, employing them to enable local dynamic control of the transmission phase for both right-circularly polarized (RCP) and left-circularly polarized (LCP) metasurface components.[49] Additionally, Tian et al. harnessed the phase-change properties of perovskites to successfully switch exciting modes. In this study, we focus on PC structures that preserve C_6 symmetry, as these structures exhibit more allowed topological charges (TCs).[50] We investigate the photonic band edge modes that are correlated with these TCs for our room temperature operated PCSELs with honeycomb and triangular lattices of the PC structures, respectively. After that, we explore the possibility of dynamic tuning of TCs. As the TCs are different among modes, the switching of TCs can be realized with lasing mode control. Specifically, we achieve mode switching by carefully regulating the junction temperature of the device through controlled injection conditions. It is noteworthy that all the previous TC switching investigations have been optically pumped, but in this study, we achieve dynamic switching within an electrically pumped semiconductor for the first time. This breakthrough represents a significant advancement in the field of PC structures and opens up new possibilities for practical applications in optoelectronic devices.

METHODS

Simple Derivation of Allowed Topological Charge in Different Symmetry Systems. As indicated in Figure 1,

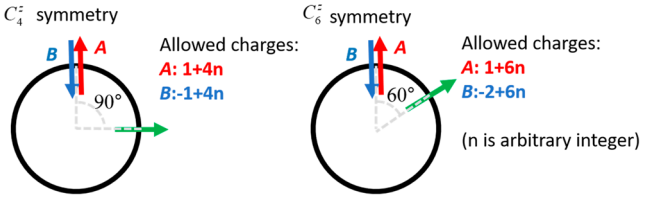

Figure 1. Figure showing how the polarization vector twists around the vortex center in *A* and *B* representations.

symmetry representations *A* and *B* are the Mulliken symbols, which stand for symmetric and antisymmetric polarization with respect to rotation around the principal rotation axis. In systems having a certain rotation symmetry *R* and without degenerate bands, the polarization vector at the transformed **k** point is equal to $\pm \mathrm{Rc}(\mathbf{k})$, the transformed polarization vector at the *k* point multiplied with +1 or −1, as proven in ref 42. Figure 1 shows how the polarization of vector vortex beams of *A* and *B* representation twists around the vortex center. For example, in systems with C_4 rotation symmetry, the polarization direction rotates ±90° as it goes from the right side (green arrow) to the upper side (red/blue arrow for *A*/*B* representation) of the vortex center. In the *A* representation, the vector could rotate 90 + 360*n* degrees, where *n* is the integer and 360*n* represents multiple 360° rotations of polarization vector. Therefore, the total twist number in a round trip around the vortex center, also known as the allowed TCs, may be 1 + 4*n*. In contrast, the polarization vector of *B* representation may rotate −90 + 360*n* degrees, resulting in allowed TCs of −1 + 4*n*. On the other hand, the possible charges in the C_6 symmetry system are 1 + 6*n* or −2 + 6*n*, corresponding to *A* and *B* representations. Table 1 shows the allowed TCs for systems with different rotation symmetry. It is worth noting that the C_3 symmetry system does not possess *B* symmetry representation because it cannot come back to the original vector after transformation of odd number times.

Table 1. Allowed Topological Charges for Systems with Different Rotation Symmetry

Symmetries	Representation	Allowed charges
C_2	*A*	1 + 2*n*
	B	0 + 2*n*
C_3	*A*	1 + 3*n*
C_4	*A*	1 + 4*n*
	B	−1 + 4*n*
C_6	*A*	1 + 6*n*
	B	−2 + 6*n*

https://doi.org/10.1021/acsphotonics.3c00561
ACS Photonics 2023, 10, 4112−4120

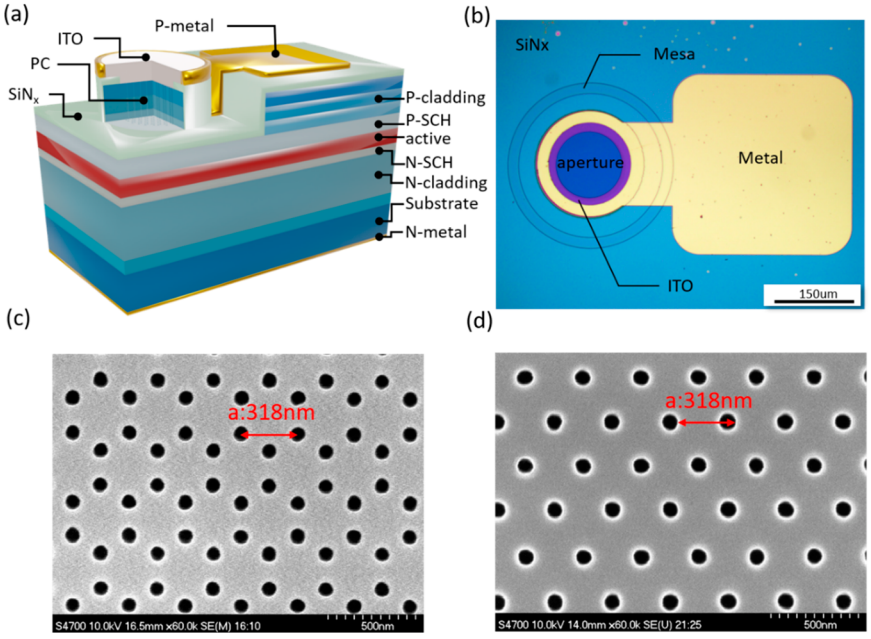

Figure 2. PCSEL structure and images of the device. (a) Schematic diagram of the designed PCSEL structure. The laser structure is mainly composed of an active layer, two SCH layers, two cladding layers, and a PC region. ITO layer is cladded on a PC for protection and current spreading purposes. (b) Top view of the OM image of the actual device. The diameters of the aperture, PC region, ITO cladding, and mesa are 120, 125, 210, and 260 μm, respectively. (c and d) Top-view SEM images of the PC structure with honeycomb (c) and hexagonal lattices (d). The black regions are etching holes that are expected to remain unfilled after ITO deposition.

Simulation Method of Polarization Vectors. The laser emissions of PCSELs with hexagonal and honeycomb lattices which preserve C_6 symmetry were investigated in our study, allowing two of the lowest TCs of +1 and −2 (n = 0). We began with evaluating the TC of the first six photonic bands through analyzing the polarization vectors in the k space. Our calculation of polarization vectors assumes an infinite device size, which overlooks the impact of the field envelope. Additionally, we simplify the model by using the effective index of the transverse mode (the mode in the epitaxial direction) to substitute for the actual 3D PCSEL structure. By applying Bloch's theorem, the electric field in a 2D photonic crystal at a resonance can be expressed in the Bloch form $\mathbf{E}_\mathbf{k}(\mathbf{r}, z) = e^{i\mathbf{k}\cdot\mathbf{r}}\mathbf{u}_\mathbf{k}(\mathbf{r}, z)$, which is the product of a plane wave and a periodic function. $\mathbf{k}$ represents the in-plane wavevector, and $\mathbf{r}$ represents the in-plane position vector (bold font is used to represent vectors). The resonances above the light line can radiate to free space in the direction corresponding to their in-plane wavevectors, and the electric field at the far field is proportional to the integral of $\mathbf{u}_\mathbf{k}$ over the near field. In general, the periodic function $\mathbf{u}_\mathbf{k}$ can be expanded into the Fourier series. As the integration range becomes large enough, only the zeroth order term counts. Hence, the polarization vector $\mathbf{c}(\mathbf{k}) = c_x(\mathbf{k})\hat{\mathbf{x}} + c_y(k)\hat{\mathbf{y}}$ can be obtained from the zeroth order term of the x- and y-components of $\mathbf{u}_\mathbf{k}$. We use the plane-wave expansion method (PWEM) to solve the governed equation:

$$\frac{1}{\varepsilon_r}(\nabla + i\boldsymbol{k}) \times (\nabla + i\boldsymbol{k}) \times \boldsymbol{u}_\boldsymbol{k} = \boldsymbol{k}_0{}^2\boldsymbol{u}_\boldsymbol{k}$$

where ε_r is dielectric constant of the simplified 2D structure. To prevent the convergence problem caused from truncation of the Fourier series, an effective tensor is used to smooth the dielectric function.[28] The orders of the Fourier series are taken from −11 to +11 in the calculation, which is large enough to get acceptable solutions.[51−53] In the C_2T system (T refers to time reversal symmetry), c_x and c_y are proven to be in-phase,[42] this indicates linear polarization at far field. The BIC arises at the specific $\mathbf{k}$-point where both c_x and c_y accidentally become zero, and the topology of this BIC can be deduced by examining the polarization's twist number around that point. The evolution of the polarization direction in $\mathbf{k}$ space of the lowest six bands is presented in Figure S1 of Supporting Information.

Device Fabrication. PCSEL devices were fabricated according to our simulation targeting the lasing mode with TC values of +1 and −2. The lasing wavelength is at around 940 nm, aligning with the gain peak of the active layer. The schematic of our PCSEL structure is shown in Figure 2(a). The PCSELs were fabricated on the epitaxial wafer grown on the n-type GaAs substrate by metal organic chemical vapor deposition (MOCVD) in sequence of a graded index (GRIN) n-$Al_{0.1-0.4}Ga_{0.9-0.6}As$ layer, a n-$Al_{0.4}Ga_{0.6}As$ cladding layer, a n-GaAs separate confinement heterostructure (SCH) layer, an active region containing 3 pairs of InGaAs/GaAs multi quantum wells (MQWs), a p-GaAs SCH layer, a p-$Al_{0.4}Ga_{0.6}As$ cladding layer, a GRIN p-$Al_{0.4-0.1}Ga_{0.6-0.9}As$ layer, and a p^+-GaAs contact layer. The PC structures of area 140 × 140 μm^2 consisting of periodic air holes were fabricated in the top three layers through e-beam lithography and a dry etching process. The etching depth was approximately 250 nm. After the PC structure formed on the epitaxial wafer, a 250-nm-thick ITO cladding layer was deposited by the electron beam (E-gun) evaporator to serve as cladding layer and current conducting layer.[54] The p-type and n-type conducting metals were deposited on ITO and the back side of the substrate, respectively, to finish the device process. An aperture was preserved on the p-type metal for output. The top view of the optical microscope (OM) image of the actual device is shown

https://doi.org/10.1021/acsphotonics.3c00561
ACS Photonics 2023, 10, 4112−4120

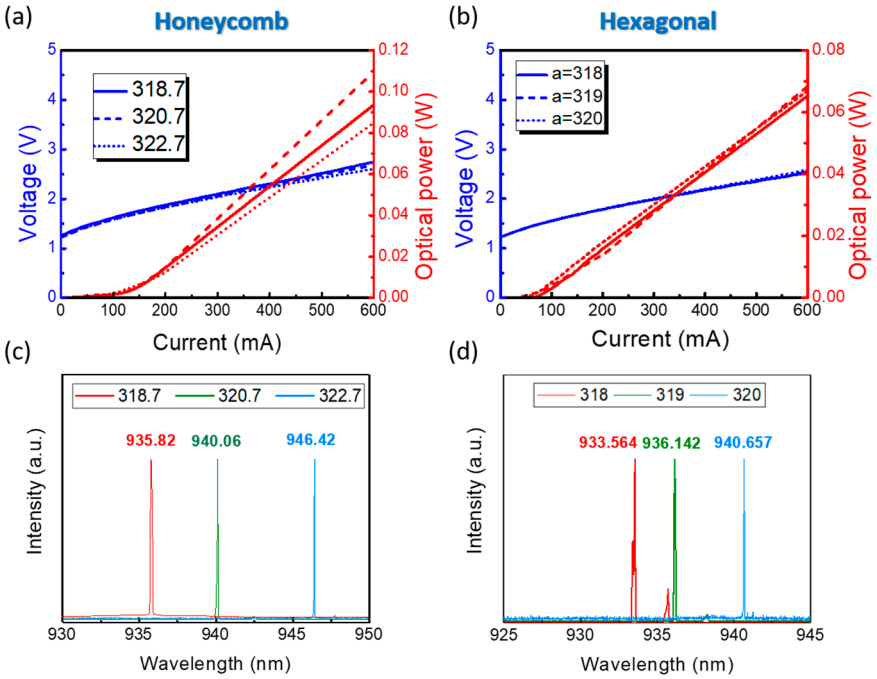

Figure 3. $L-I-V$ characteristics and spectra. (a, b) Measured $L-I-V$ curves of Hon-PCSEL (a) and Hex-PCSEL (b) under pulsed electrical pumping. The different line styles stand for different PC lattice constants. (c and d) Measured emission spectra of Hon-PCSEL (c) and Hex-PCSEL (d). The different colors stand for different PC lattice constants. The maximum intensity has been normalized to the same value.

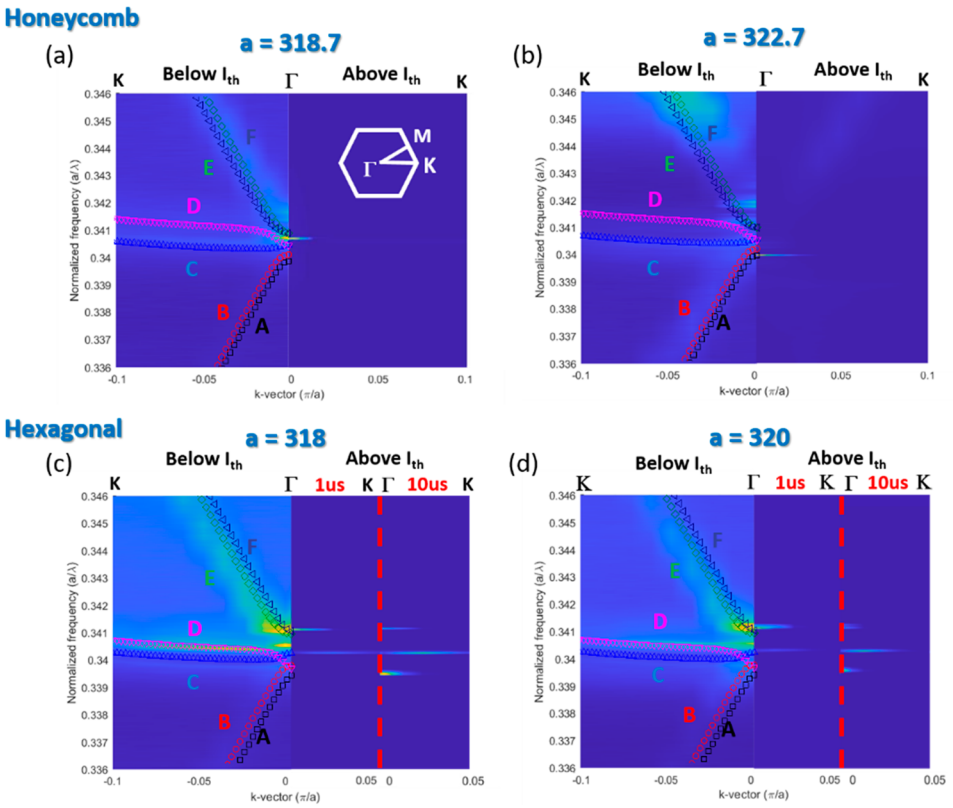

Figure 4. AREL spectra below (left) and above (right) the lasing threshold of (a) Hon-PCSELs with a lattice constant of 318.7 nm, (b) Hon-PCSELs with a lattice constant of 322.7 nm, (c) Hex-PCSELs with a lattice constant of 318 nm, and (d) Hex-PCSELs with a lattice constant of 320 nm. The upper-right inset in (a) is the first Brillouin zone of the reciprocal lattice. The AREL measurements are conducted along the Γ-M direction. The Hon-PCSELs are measured with the pulse duration 1 μs and duty cycle 0.1%, while the Hex-PCSELs are additionally measured with a pulse duration 10 μs above the threshold. The scattered points are the TE and TM photonic bands calculated by the PWEM method. We define the modes with low to high frequencies as the A ∼ F modes.

https://doi.org/10.1021/acsphotonics.3c00561
ACS Photonics 2023, 10, 4112−4120

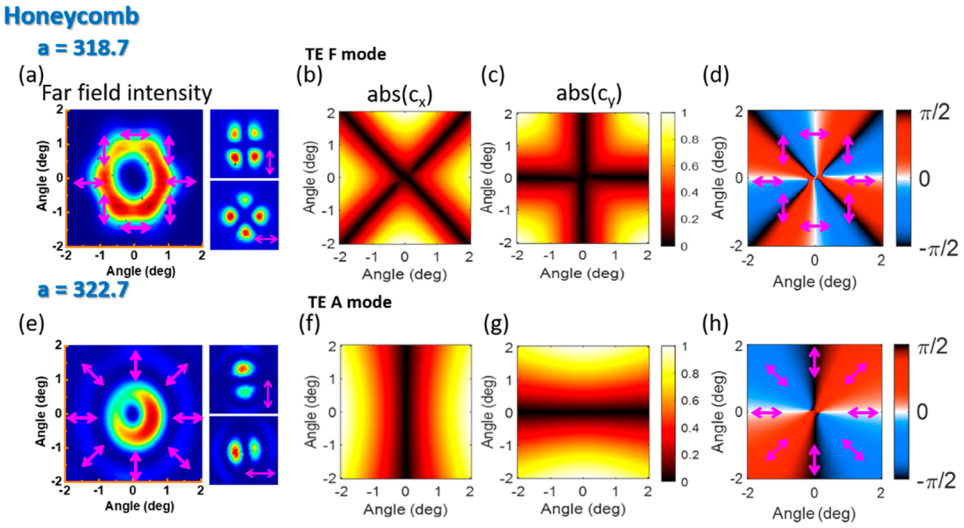

Figure 5. Far-field pattern and polarization direction of PCSELs with a honeycomb lattice. (a) Measured FFP of Hon-PCSEL with the lattice constant 318.7 nm. The pink arrows represent the polarization directions. The figures in the right panel depict the measured FFPs with the polarizer oriented along the pink arrows. The TC is identified to be −2. (b and c) The calculated magnitudes of the *x*- and *y*-components of the polarization vector of the TE F mode. The black lines represent zero intensity of this component. (d) Orientation of the electric field of the TE F mode at different **k** points. The orientation is indicated by its azimuthal angle (radian) relative to the *x*-axis. The TE F mode shows a TC of −2. (e−h) Measured FFP, calculated magnitude, and orientation of electric field for Hon-PCSEL with the lattice constant 322.7 nm. The TC is identified to be +1 and is consistent with the TE A mode in the calculation.

in Figure 2(b). The diameters of the aperture, PC region, ITO cladding, and mesa are 120, 125, 210, and 260 μm, respectively. The top views of the PC lattices are shown in Figures 2(c) and 2(d), corresponding to hexagonal and honeycomb lattices. The honeycomb lattice is a special case of a hexagonal lattice with a two-hole basis. For each type of lattice, we design 3 different lattice constants for comparison. The designed lattice constants of the honeycomb lattice are 318.7, 320.7, and 322.7 nm, while they are 318, 319, and 320 nm for the hexagonal lattice. The filling factor, defined as the area ratio of the air hole, is 0.09 and 0.05 for the honeycomb and hexagonal lattices, respectively.

RESULTS AND DISCUSSION

The $L-I-V$ characteristics and lasing spectra of the PCSELs are depicted in Figure 3. The measurements were conducted in the pulse mode with a pulse duration of 1 μs and duty cycle of 0.1%. All the samples show similar $I-V$ characteristics with a turn-on voltage of about 1.25 V and a serial resistance of about 2 ohms. The threshold currents of PCSELs with honeycomb lattices (Hon-PCSELs) and PCSELs with hexagonal lattices (Hex-PCSELs) are around 130 and 60 mA, respectively. The close threshold current of PCSELs with different lattice constants can be attributed to the relatively flat gain peak near these lasing wavelengths. The higher threshold current in Hon-PCSELs is attributed to the cancellation of in-plane feedback of the two-hole basis in the honeycomb lattice and larger radiation loss from the stronger first-order diffraction. Slope efficiencies range from 0.146 to 0.180 W/A in the honeycomb lattice and 0.125 to 0.130 W/A in the hexagonal lattice. The slope efficiencies of PCSELs with different lattice constants are thought to be similar because of the same filling factor of PC and thus the same components of optical loss. The deviation may come from the fabrication process and gain mode offset. The obvious higher slope efficiency in the honeycomb lattice is related to the larger radiation loss ratio. The lasing wavelengths are near the design at 940 nm and increase with respect to the lattice constant at a ratio of about 3.

We have identified the lasing mode through comparison of the measured band diagram, lasing spectra, and calculated photonic band diagram, as shown in Figure 4. The band diagram can be measured by conducting angle-resolved electroluminescence (AREL) measurements of spectra below the lasing threshold. Here we scan along the Γ-M direction. The scattered points are the band calculated by the PWEM. The lasing modes in our devices are expected to exhibit TE polarization, which refers to the oscillation modes in which the electric field is predominantly parallel to the epitaxial layer. This judgment is attributed to the significant enhancement of the TE mode when subjected to in-plane compressive strain in InGaAs MQWs. Therefore, our discussion will focus on the TE modes due to their favorable response to the applied strain. At the frequency near Γ, there exist six modes for TE polarization, owing to the C_6 symmetry. We define the modes from low to high frequency as A ∼ F modes. It is important to mention that the A/B mode described here should not be confused with the A/B representation above. In Hon-PCSELs with lattice constants of 318.7 and 320.7 nm (not shown in the figure), the lasing occurred near the E and F modes. In contrast, the lasing of Hon-PCSEL with lattice constant of 322.7 nm occurred near the A ∼ D modes.

On the other hand, in Hex-PCSELs, we found that a third peak appears as the pulse duration increases. The measurement results under 1 and 10 μs are both shown in Figures 4(c) and 4(d) for comparison. The lasing behavior is similar, with different lattice constants in the Hex-PCSEL. There are two peaks at the pulse duration of 1 μs, corresponding to the multipeaks shown in Figure 3(d). The top peak is near the E and F modes, while the second is near the C and D modes. Once the pulse duration is increased to 10 μs, a bottom peak lasing near the A and B modes appears. The comparison of the

https://doi.org/10.1021/acsphotonics.3c00561
ACS Photonics 2023, 10, 4112−4120

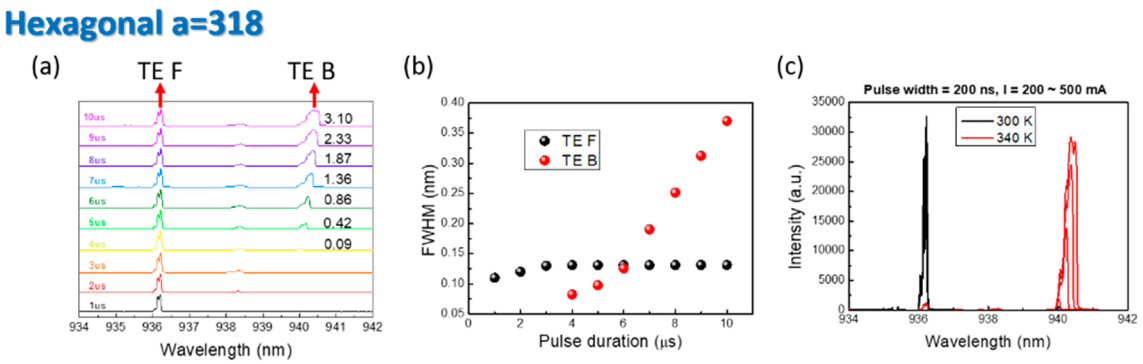

Figure 6. (a) measured spectra of Hex-PCSEL with the lattice constant 318 nm under different pulse duration conditions, where the repetition rate is fixed to be 1 kHz. The numbers on the right-hand side represent the ratio of integrated power of the TE B mode relative to the TE F mode. (b) The fwhm of the two main peaks in (a). (c) Spectra measured with the heat plate temperatures 300 and 340 K. The pulse width is fixed to be 200 ns, and the current is ranging from 200 to 500 mA.

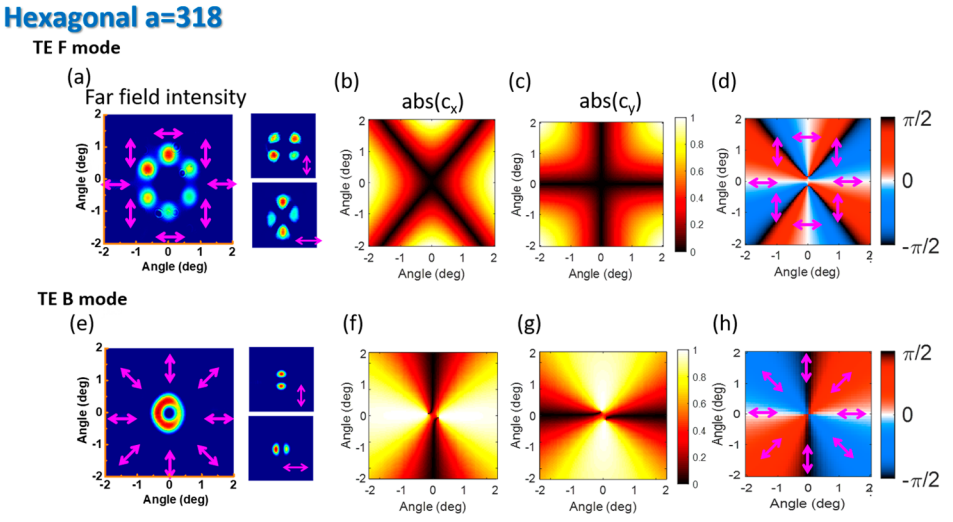

Figure 7. (a and e) Measured FFPs of Hex-PCSELs under 1 and 10 μs pulse duration conditions. The figures in the right panel depict the measured FFPs with the polarizer oriented along the pink arrows. The TC is −2 in the 1 μs case, while it becomes +1 in the 10 μs case. (b−e and f−h) Calculation results of the TE F mode and the TE B mode of Hex-PCSELs.

band diagram and lasing peak offers a rough identification on the lasing mode. In the next part, we will compare their polarization states and verify that the measurement results are consistent with the calculated results.

Figure 5(a) shows the far-field pattern (FFP) of Hon-PCSELs with a lattice constant of 318.7 nm. The pink arrows represent the polarization directions. The measured FFPs with a polarizer oriented along 0° and 90° are shown in the right panel of Figure 5(a). FFPs acquired with the polarizer set at different angles can be found in Figure S2 in the Supporting Information. It should be mentioned, in the case of VBs, that their distinctive feature is the twisting of the phase front, which necessitated an interference experiment for demonstration.[55] On the other hand, VVBs have their uniqueness in the twisting of polarization. In this case, the polarization information along the azimuthal angle offers more direct evidence to confirm the presence of VVBs. The FFPs measured with a polarizer show that the polarization twists two times along the azimuthal angle with the inverse direction of the polarizer, indicating the *B* representation with a TC of −2. We compare the measured results with the calculation and find it consistent with the TE F mode. The calculated magnitudes of the *x*- and *y*-components of the polarization vector (c_x and c_y) of the TE F mode are shown in Figure 5(b) and 5(c). The black nodal lines represent zero intensity of this component at the **k** points along the lines. BICs form when both c_x and c_y become zero. The laser emission around the intersection will form a vector vortex, and the order increases as the number of nodal lines crossing it increases. Figure 5(d) shows the orientation of the electric field, as indicated by its azimuthal angle (in radian) relative to the *x*-axis. Each 2π variation along the azimuthal angle results in one twist of polarization. The TE F mode shows a TC of −2 and is consistent with the experiment results in both the spectrum and polarization.

In contrast, Figure 5(e) shows the FFP of Hon-PCSELs with a lattice constant of 322.7 nm. In this case, the polarization twists only once and is in the same direction as the polarizer, indicating *A* representation with the TC of +1, which is consistent with the TE A mode in the calculation. Despite some simplifications, the simulation method accurately predicts the behavior of PCSELs and allows for rapid selection of the desired OAM order.

On the other hand, the Hex-PCSEL samples perform the same FFP and polarization with different lattice constants.

https://doi.org/10.1021/acsphotonics.3c00561
ACS Photonics 2023, 10, 4112−4120

However, they exhibit different FFP and polarization while the pulse duration is extended. Therefore, we conducted the analysis on different pulse conditions rather than on lattice constants. Figure 6(a) shows the measured emission spectra of Hex-PCSEL (lattice constant of 318 nm) versus different pulse duration conditions, where the repetition rate is fixed at 1 kHz. As the pulse duration increases from 1 to 10 μs, a third mode appears. The mode competition in Hex-PCSELs is believed to be caused by the smaller threshold gain difference, which is supported by the threshold gain simulations as shown in Figure S4 of the Supporting Information. As the pulse duration increases, the junction temperature in the semiconductor laser also rises, causing a red-shift in the gain peak. This shift leads to mode hopping from shorter to longer wavelengths. For further insights into the time-dependent thermal simulation and the associated mode and gain peak shifts, please refer to Figure S6. The information on the full-width at half-maximum (fwhm) of the lasing line width with respect to the pulse duration is shown in Figure 6(b) for reference. As we will clarify later, the two peaks correspond to the TE F and TE B modes. These two modes have different TCs, and switching between them allows for TC control.

The power ratio between the two modes was found to be approximately 3.1 with a pulse duration of 10 μs. By extending the pulse duration further, the TE B mode can thoroughly dominate the output power. However, due to concerns about potential damage to the metal pad, the pulse duration is currently limited to 10 μs. This limitation can be addressed through the implementation of a suitable metal pad design, which poses no challenges to mature manufacturing technology. To demonstrate the total transition between the two modes, the temperature of the heat plate in contact with the *n*-metal pad was varied instead. In Figure 6(c), spectra are presented for heat plate temperatures of 300 and 340 K, with current levels ranging from 200 to 500 mA. To mitigate the self-heating effect in the junction, the pulse duration was reduced to 200 ns. The results show a high power ratio between the two modes at both temperatures, indicating that an injection current of 1 A and pulse duration above 15 μs could be enough to achieve a complete mode switching.

In Figures 7(a) and 7(e), we again present the FFPs measured without a polarizer (left panel) and with a polarizer (right panel) corresponding to pulse durations of 1 and 10 μs, respectively. For FFPs measured with other polarizer orientations, please refer to Figure S3 in the Supporting Information. Through the measurements, we observed that the TC was −2 in the 1 μs case but became +1 in the 10 μs case. The measured polarizations were consistent with the simulation results of the TE F and TE B modes, respectively. Remarkably, the modulation of orbital angular momentum (OAM) depended on the current injection condition without the need for any mechanical parts and exhibited a response time on the order of μs. Additionally, by adjusting the design of the photonic crystal geometry and the lasing band, we clearly demonstrated the ability to switch between other OAMs.

Moreover, we investigated the PCSEL with C_2 symmetry by introducing perturbations on the hexagonal lattice. From the AREL measurement, the lasing peak is identified as the TE E or TE F mode. The measured charge of the resulting output beam is +1 and azimuthally polarized. The decreased charge is a result from the elimination of the double degeneracy of the nodal lines c_x and c_y at the Γ-point. The TC is invariant to changes in the lattice constant and injection conditions. Breaking the symmetry provides a method for generating a consistent TC. The details of applied perturbation and measurement results are presented in Figure S6.

CONCLUSION

In conclusion, we have demonstrated the generation and manipulation of vector vortex beams with different TCs using our Hex-PCSELs and Hon-PCSELs, which is in good agreement with our simulation results. Through the experiments, we obtained an in-depth understanding of the generation and manipulation of vortex laser beams via electrically driven PCSELs. Hex-PCSELs exhibit a tendency for their modes to switch, whereas the modes in Hon-PCSELs are comparatively more stable. Our findings provide insights into the topological nature of photonic crystal structures and their potential applications in information processing and other fields that require the manipulation of light beams. Moreover, by fine-tuning the device structure or the driving current, we can manipulate the TCs of the beams, which opens up new possibilities for the development of more sophisticated optical communication systems and other applications. The results obtained from our experiments represent a significant advancement in the field of PCSELs and may pave the way for the development of smaller and more versatile devices.

ASSOCIATED CONTENT

Data Availability Statement

Data underlying the results presented in this paper are not publicly available at this time but may be obtained from the authors upon reasonable request.

Supporting Information

The Supporting Information is available free of charge at https://pubs.acs.org/doi/10.1021/acsphotonics.3c00561.

Additional polarization simulation results in k-space, FFP measured with a polarizer, and self-interference measurement results (PDF)

AUTHOR INFORMATION

Corresponding Author

Tien-Chang Lu − *Department of Photonics, College of Electrical and Computer Engineering, National Yang Ming Chiao Tung University, Hsinchu 30010, Taiwan;* orcid.org/0000-0003-4192-9919; Email: timtclu@nycu.edu.tw

Authors

Chia-Jui Chang − *Department of Photonics, College of Electrical and Computer Engineering, National Yang Ming Chiao Tung University, Hsinchu 30010, Taiwan;* orcid.org/0000-0002-1897-4802

Yu-Wen Chen − *Department of Photonics, College of Electrical and Computer Engineering, National Yang Ming Chiao Tung University, Hsinchu 30010, Taiwan*

Lih-Ren Chen − *Department of Photonics, College of Electrical and Computer Engineering, National Yang Ming Chiao Tung University, Hsinchu 30010, Taiwan;* orcid.org/0000-0002-4819-3337

Kuo-Bin Hong − *Semiconductor Research Center, Hon Hai Research Institute, Taipei City 23678, Taiwan;* orcid.org/0000-0001-5027-6273

https://doi.org/10.1021/acsphotonics.3c00561
ACS Photonics 2023, 10, 4112−4120

Jhih-Sheng Wu − *Department of Photonics, College of Electrical and Computer Engineering, National Yang Ming Chiao Tung University, Hsinchu 30010, Taiwan*

Yao-Wei Huang − *Department of Photonics, College of Electrical and Computer Engineering, National Yang Ming Chiao Tung University, Hsinchu 30010, Taiwan;* orcid.org/0000-0001-8983-413X

Complete contact information is available at: https://pubs.acs.org/10.1021/acsphotonics.3c00561

Notes

The authors declare no competing financial interest.

■ ACKNOWLEDGMENTS

This work was financially supported by Taiwan's National Science and Technology Council under Contract Nos. MOST 110-2221-E-A49-058-MY3 and MOST 110-2622-8-A49-008-SB and partially supported by Hon Hai Research Institute. Y.-W.H. acknowledges support from the Ministry of Science and Technology in Taiwan (Grant No. 110-2112-M-A49-034-MY3) and support from the Ministry of Education in Taiwan under the Yushan Young Scholar Program.

■ REFERENCES

(1) Allen, L.; Beijersbergen, M. W.; Spreeuw, R. J.; Woerdman, J. P. Orbital angular momentum of light and the transformation of Laguerre-Gaussian laser modes. *Phys. Rev. A* **1992**, *45* (11), 8185.

(2) He, H.; Friese, M. E.; Heckenberg, N. R.; Rubinsztein-Dunlop, H. Direct observation of transfer of angular momentum to absorptive particles from a laser beam with a phase singularity. *Phys. Rev. Lett.* **1995**, *75* (5), 826.

(3) Mair, A.; Vaziri, A.; Weihs, G.; Zeilinger, A. Entanglement of the orbital angular momentum states of photons. *Nature* **2001**, *412* (6844), 313−316.

(4) Wang, J.; Yang, J. Y.; Fazal, I. M.; Ahmed, N.; Yan, Y.; Huang, H.; Willner, A. E. Terabit free-space data transmission employing orbital angular momentum multiplexing. *Nat. Photonics* **2012**, *6* (7), 488−496.

(5) Gibson, G.; Courtial, J.; Padgett, M. J.; Vasnetsov, M.; Pas'ko, V.; Barnett, S. M.; Franke-Arnold, S. Free-space information transfer using light beams carrying orbital angular momentum. *Opt. Express* **2004**, *12* (22), 5448−5456.

(6) Wang, Y.; Zhang, J.; Ren, Y.; Cheng, L.; Zhu, B.; Zhao, Z. Demonstration of high-speed free-space optical communication using orbital angular momentum (OAM) modes. *Opt. Commun.* **2018**, *426*, 327−332.

(7) Goyal, S. K.; Roux, F. S.; Forbes, A. Theoretical and experimental study of bit error rate performance of a spatially multiplexed free-space optical communication system using multiple orbital angular momentum modes. *Opt. Express* **2012**, *20* (13), 1405−1419.

(8) Lavery, M. P. J.; Speirits, F. C.; Barnett, S. M.; Padgett, M. J. Detection of a spinning object using light's orbital angular momentum. *Science* **2013**, *341* (6145), 537−540.

(9) Qiu, S.; Liu, T.; Li, Z.; Wang, C.; Ren, Y.; Shao, Q.; Xing, C. Influence of lateral misalignment on the optical rotational Doppler effect. *Appl. Opt.* **2019**, *58* (10), 2650.

(10) Schmiegelow, C. T.; Schulz, J.; Kaufmann, H.; Ruster, T.; Poschinger, U. G.; Schmidt-Kaler, F. Transfer of optical orbital angular momentum to a bound electron. *Nat. Commun.* **2016**, *7* (1), 129.

(11) Grier, D. G. A revolution in optical manipulation. *Nature* **2003**, *424* (6950), 810.

(12) Moffitt, J.; Chemla, Y.; Smith, S. B.; Bustamante, C. Recent advances in optical tweezers. *Annu. Rev. Biochem.* **2008**, *77*, 205−2.

(13) Ashkin, A.; Dziedzic, J. M. Optical trapping and manipulation of viruses and bacteria. *Science* **1987**, *235* (4795), 1517.

(14) Ashkin, A.; Dziedzic, J. M.; Bjorkholm, J. E.; Chu, S. Observation of a single-beam gradient force optical trap for dielectric particles. *Opt. Lett.* **1986**, *11* (5), 288−90.

(15) Pinheiro da Silva, B.; Buono, W. T.; Pereira, L. J.; Tasca, D. S.; Dechoum, K.; Khoury, A. Z.. Spin to orbital angular momentum transfer in nonlinear wave mixing. *Frontiers in Optics*; Optica Publishing Group, 2022. (Accessed 2023-10-17).

(16) D'Ambrosio, V.; Carvacho, G.; Graffitti, F.; Vitelli, C.; Piccirillo, B.; Marrucci, L.; Sciarrino, F. Entangled vector vortex beams. *Phys. Rev. A* **2016**, *94* (3), 030304.

(17) Naidoo, D.; Roux, F. S.; Dudley, A.; Litvin, I.; Piccirillo, B.; Marrucci, L.; Forbes, A. Controlled generation of higher-order Poincaré sphere beams from a laser. *Nat. Photonics* **2016**, *10* (5), 327−332.

(18) Li, Y.; Li, J.; Lü, B. Needle beam generation from an azimuthally polarized beam using a phase-only zone plate. *Opt. Lett.* **2017**, *42* (4), 771−774.

(19) Delaney, S.; Sanchez-Lopez, M. M.; Moreno, I.; Davis, J. A. Arithmetic with q-plates. *Appl. Opt.* **2017**, *56* (3), 596−600.

(20) Machavariani, G.; Lumer, Y.; Moshe, I.; Meir, A.; Jackel, S. Spatially-variable retardation plate for efficient generation of radiallyand azimuthally-polarized beams. *Opt. Commun.* **2008**, *281*, 732−738.

(21) Cardano, F.; Karimi, E.; Slussarenko, S.; Marrucci, L.; de Lisio, C.; Santamato, E. Polarization pattern of vector vortex beams generated by q-plates with different topological charges. *Appl. Opt.* **2012**, *51*, C1−C6.

(22) Wang, X. L.; Ding, J.; Ni, W. J.; Guo, C. S.; Wang, H. T. Generation of arbitrary vector beams with a spatial light modulator and a common path interferometric arrangement. *Opt. Lett.* **2007**, *32*, 3549−3551.

(23) Rong, Z. Y.; Han, Y. J.; Wang, S. Z.; Guo, C. S. Generation of arbitrary vector beams with cascaded liquid crystal spatial light modulators. *Opt. Express* **2014**, *22*, 1636−1644.

(24) Lim, B. C.; Phua, P. B.; Lai, W. J.; Hong, M. H. Fast switchable electro-optic radial polarization retarder. *Opt. Lett.* **2008**, *33*, 950−952.

(25) Mushiake, Y.; Matsumura, K.; Nakajima, N. Generation of radially polarized optical beam mode by laser oscillation. *Proc. IEEE* **1972**, *60*, 1107−1109.

(26) Naidoo, D.; Aït-Ameur, K.; Brunel, M.; Forbes, A. Intra-cavity generation of superpositions of Laguerre−Gaussian beams. *Appl. Phys. B: Laser Opt.* **2012**, *106*, 683−690.

(27) Tidwell, S. C.; Ford, D. H.; Kimura, W. D. Generating radially polarized beams interferometrically. *Appl. Opt.* **1990**, *29*, 2234−2239.

(28) Passilly, N.; Treussart, F.; Hierle, R.; de Saint Denis, R.; Ait-Ameur, K.; Roch, J.-F. Simple interferometric technique for generation of a radially polarized light beam. *J. Opt. Soc. Am. A* **2005**, *22* (984), 984−991.

(29) Khonina, S. N.; Karpeev, S. V.; Alferov, S. V. Polarization converter for higher-order laser beams using a single binary diffractive optical element as beam splitter. *Opt. Lett.* **2012**, *37* (2385), 2385−2391.

(30) Yue, F.; Wen, D.; Xin, J.; Gerardot, B. D.; Li, J.; Chen, X. Vector Vortex Beam Generation with a Single Plasmonic Metasurface. *ACS Photonics* **2016**, *3* (9), 1558−1563.

(31) Xu, Y.; Zhang, H.; Li, Q.; Zhang, X.; Xu, Q.; Zhang, W.; Hu, C.; Zhang, X.; Han, J.; Zhang, W. Generation of terahertz vector beams using dielectric metasurfaces via spin-decoupled phase control. *Nanophotonics* **2020**, *9* (10), 3393−3402.

(32) Liu, Y.; Ke, Y.; Zhou, J.; Liu, Y.; Luo, H.; Wen, S.; Fan, D. Generation of perfect vortex and vector beams based on Pancharatnam-Berry phase elements. *Sci. Rep.* **2017**, *7*, 44096.

(33) Zeng, J.; Li, L.; Yang, X.; Gao, J. Generating and Separating Twisted Light by gradient-rotation Split-Ring Antenna Metasurfaces. *Nano Lett.* **2016**, *16*, 3101−3108.

(34) Zeng, J.; Luk, T. S.; Gao, J.; Yang, X. Spiraling light with magnetic metamaterial quarter-wave turbines. *Sci. Rep.* **2017**, *7*, 11824.
(35) Yi, X.; Ling, X.; Zhang, Z.; Li, Y.; Zhou, X.; Liu, Y. Generation of cylindrical vector vortex beams by two cascaded metasurfaces. *Opt. Express* **2014**, *22* (17207), 17207−17215.
(36) Liu, Z.; Liu, Y.; Ke, Y.; Liu, Y.; Shu, W.; Luo, H. Generation of arbitrary vector vortex beams on hybrid-order Poincaré sphere. *Photonics Res.* **2017**, *5* (1), 15−21.
(37) He, Y.; Li, Y.; Liu, J.; Zhang, X.; Cai, Y.; Chen, Y.; Chen, S.; Fan, D. Switchable phase and polarization singular beams generation using dielectric metasurfaces. *Sci. Rep.* **2017**, *7* (1), 6814.
(38) He, Y.; Ye, H.; Liu, J.; Xie, Z.; Zhang, X.; Xiang, Y. Order-controllable cylindrical vector vortex beam generation by using spatial light modulator and cascaded metasurfaces. *IEEE Photon J.* **2017**, *9* (5), 6101710.
(39) Wang, S.; Liu, Y.; Yang, S. A.; Lei, D. Y. Multifunctional vector beam generation using metasurface. *Appl. Phys. Lett.* **2019**, *114* (12), 121103.
(40) Fu, P.; Ni, P.-N.; Wu, B.; Pei, X.-Z.; Wang, Q.-H.; Chen, P.-P.; Xu, C.; Kan, Q.; Chu, W.-G.; Xie, Y.-Y. Metasurface Enabled On-Chip Generation and Manipulation of Vector Beams from Vertical Cavity Surface-Emitting Lasers. *Adv. Mater.* **2023**, *35* (12), 2204286.
(41) Cai, X.; Wang, J.; Strain, M. J.; Johnson-Morris, B.; Zhu, J.; Sorel, M.; O'Brien, J. L.; Thompson, M. G.; Yu, S. Integrated Compact Optical Vortex Beam Emitters. *Science* **2012**, *338* (6105), 363−366.
(42) Zhen, B.; Hsu, C. W.; Lu, L.; Stone, A. D.; Soljacic, M. Topological Nature of Optical Bound States in the Continuum. *Phys. Rev. Lett.* **2014**, *113*, 257401.
(43) Yoda, T.; Notomi, M. Generation and Annihilation of Topologically Protected Bound States in the Continuum and Circularly Polarized States by Symmetry Breaking. *Phys. Rev. Lett.* **2020**, *125*, 053902.
(44) Iwahashi, S.; Kurosaka, Y.; Sakai, K.; Kitamura, K.; Takayama, N.; Noda, S. Higher-order vector beams produced by photonic-crystal lasers. *Opt. Exp.* **2011**, *19*, 11963.
(45) Kodigala, A.; Lepetit, T.; Gu, Q.; Bahari, B.; Fainman, Y.; Kante, B. Lasing action from photonic bound states in continuum. *Nature* **2017**, *541* (7636), 196−199.
(46) Doeleman, H. M.; Monticone, F.; den Hollander, W.; Alù, A.; Koenderink, A. F. Experimental observation of a polarization vortex at an optical bound state in the continuum. *Nat. Photonics* **2018**, *12*, 397−401.
(47) Wang, B.; Liu, W.; Zhao, M.; Wang, J.; Zhang, Y.; Chen, A.; Guan, F.; Liu, X.; Shi, L.; Zi, J. Generating optical vortex beams by momentum-space polarization vortices centered at bound states in the continuum. *Nat. Photonics* **2020**, *14*, 623.
(48) Huang, C.; Zhang, C.; Xiao, S.; Wang, Y.; Fan, Y.; Liu, Y.; Zhang, N.; Qu, G.; Ji, H.; Han, J.; Ge, L.; Kivshar, Y.; Song, Q. Ultrafast control of vortex microlasers. *Science* **2020**, *367*, 1018.
(49) Cai, Z.; Wu, C.; Jiang, J.; Ding, Y.; Zheng, Z.; Ding, F. Phase-change metasurface for switchable vector vortex beam generation. *Optics Express* **2021**, *29* (26), 42762−42771.
(50) Tian, J.; Adamo, G.; Liu, H.; Wu, M.; Klein, M.; Deng, J.; Ang, N. S. S.; Paniagua-Dominguez, R.; Liu, H.; Kuznetsov, A. I.; Soci, C. Phase-Change Perovskite Microlaser with Tunable Polarization Vortex. *Adv. Mater.* **2023**, *35*, 2207430.
(51) Shi, S.; Chen, C.; Prather, D. W. Plane-wave expansion method for calculating band structure of photonic crystal slabs with perfectly matched layers. *J. Opt. Soc. Am.* **2004**, *21* (9), 1769−1775.
(52) Cao, Y.; Hou, Z.; Liu, Y. Convergence problem of plane-wave expansion method for phononic crystals. *Phys. Lett. A* **2004**, *327* (2−3), 247−253.
(53) David, A.; Benisty, H.; Weisbuch, C. Fast factorization rule and plane-wave expansion method for two-dimensional photonic crystals with arbitrary hole-shape. *Phys. Rev. B* **2006**, *73*, 075107.
(54) Huang, S.-C.; Hong, K.-B.; Chiu, H.-L.; Lan, S.-W.; Chang, T.-C.; Li, H.; Lu, T.-C. Design of photonic crystal surface emitting lasers with indium-tin-oxide top claddings. *Appl. Phys. Lett.* **2018**, *112* (6), 1105.
(55) Miao, P.; Zhang, Z.; Sun, J.; Walasik, W.; Longhi, S.; Litchinitser, N. M.; Feng, L. Orbital angular momentum microlaser. *Science* **2016**, *353*, 464−467.

https://doi.org/10.1021/acsphotonics.3c00561
ACS Photonics 2023, 10, 4112−4120